Chapter 5 Influence of Dopants on Hydrothermal growth ZnO Nanowires

5.1 Influence of Mg Dopant on ZnO Nanowires
5.1.1 Structural analysis

The AFM photographs shown in Fig. 5.1 reveal the initial nucleation of hydrothermal growth. Figure 5.1 (a) depicts the AFM image of the 70 Å thick rf–sputtered ZnO film, indicating that the grain size and surface roughness of this film are about 50, and 0.837 nm, respectively. This rf-sputtered ZnO film served as a seeding layer for the following ZnO NWs hydrothermally grown on the substrate. Then, these coated substrates were put in the aqueous solution A of $Zn(NO_3)_2 \cdot 6H_2O$ and HMTA and B of $Zn(NO_3)_2 \cdot 6H_2O$, HMTA and $Mg(NO_3)_2 \cdot 6H_2O$ (0.02 M) at 85 ^oC for 10 min. in the sealed vessels, respectively, to observe the influence of Mg on the initial nucleation. The surface morphology of the sample put in the solution A, shown as figure 5.1 (b), indicates the surface grain size of 250 nm and surface roughness of 11.52 nm, while the surface morphologies of the sample put in the solution B (Figure 5.1 (c)) are round surface grains with a grain size of 80 nm and surface roughness of 75.93 nm. Such different morphologies, which arise from different nucleation–growth mechanism, may be explained by the different surface energy between ZnO and MZO that leads to the formation of ZnO film on the surface of coated substrate in the solution A, and the islands of MZO are formed on the substrate surface in the solution B.

The cross–section FE-SEM image of ZnO NWs immediately grown on the ITO glass substrate before cleaning shown in Fig. 5.2 (a) depicts that some impurities, probably including $Zn(NO_3)_2$, HMTA and ZnO crystal appear on the top of NWs.

Therefore, we cleaned such a 2h synthesized NWs with DI water to remove those impurities and dried in the vacuum oven for 5 h. After cleaning, there are no impurities on the top of NWs as shown in Fig. 5.2(b). Thus, we employed above cleaning process for all of the grown NWs. The FE–SEM images of MZO NWs ($0 \leq x \leq 0.25$) on glass substrates are shown in Figs. 5.2(b) to (g), indicating that the surface morphologies of these MZO NWs depend on the amount of Mg. The chemical composition of these NWs was confirmed by the EDX attached with the FE–SEM (not shown here). This analysis was focused on the individual NWs to avoid the influence of underlying ZnO layer. As shown in Fig. 5.2 (b), a 200 nm thick ZnO film deposited on the glass substrate during hydrothermal growth and well–aligned ZnO NWs grown on such a ZnO film have acicular tips with a diameter of 50 nm and length of 0.5 μm. This ZnO film is thicker than the rf–sputtered seeding layer. Such a thick ZnO film which gradually regulates the orientation on the substrate is suitable for the well–aligned growth of ZnO NWs. The NWs have fewer number density since some precursors were consumed during the ZnO film deposition. On the contrary, the MZO ($0.05 \leq x \leq 0.20$) NWs grown on thinner films have blunt tips, slender roots, larger number density and random distribution (Figs. 5.2 (c), (d), and (e)). The films hydrothermally grown on the coated substrates are thinner, and composed of columnar grains. This polycrystalline film with the distinct orientation results in the non–vertical random distribution growth of MZO NWs. The MZO NWs grow larger in sizes by the addition of Mg in the aqueous solution. The average diameter of these MZO NWs is from 80 to 100 nm and the length is from 0.5 to 1 μm. The larger MZO NWs may be attributed to the larger part of the precursor being consumed during the MZO NWs growth as compared with the ZnO film growth. The surface energy difference between ZnO and MZO also affects the geometry of these NWs, which was demonstrated in Fig. 5.1. The ZnO NWs have a uniform diameter in stems, while the

MZO NWs have larger diameter in stems and narrow roots on the substrate. The MZO NWs were grown on the MZO islands formed on the seeding layer in the initial stage of hydrothermal process which leads to the formation of narrow roots of MZO NWs on the substrate after reaction. In this solid solution process, the Mg atoms substitute the Zn sites. As the Mg content is increased to 0.25, the growth of MZO NWs slows down. The diameter of these MZO NWs ranges between 80 and 100 nm, and the length of these is reduced to 150 nm. Due to the difference in the radii of Mg^{2+} and Zn^{2+} ions, the solubility of Mg in the ZnO NWs decides the upper limitation of the hydrothermal growth.

Figure 5.3 (a) shows the XRD patterns of MZO NWs with various Mg content. Single phase MZO NWs could be synthesized with x up to 0.25 by hydrothermal method. With the increase in Mg content of the MZO NWs, it is observed that the crystal structures of these NWs are wurtzite type and no other impurities appear. As shown in the figure, the peak intensity of MZO NWs (x = 0.25) is smaller than others for there are fewer NWs grown on the substrate. Lattice constant and corresponding cell volume measured from the XRD patterns are shown as a function of the Mg content in Fig. 5.3 (b). With the increase of Mg content from 0 to 0.25, the c–axis lengths calculated from the (0002) peak of the NWs decrease from 5.21 to 5.17 Å, while a–axis lengths calculated from the ($2\bar{1}\bar{1}0$) increase from 3.23 to 3.25 Å. However, the cell volumes of these NWs are almost unchanged. The addition of MgO to ZnO forms a solid solution with the wurtzite structure, and the deviation of the lattice constants can be due to the small difference of ionic radii of Mg^{2+} and Zn^{2+}.

HR–TEM images and corresponding selected area electron diffraction (SAED) are shown in Fig. 5.4, which illustrates the appearance and crystal structure of the NWs. The ZnO NW (Figs. 5.4 (a), and (b)) with a acicular tip, uniform diameter of 50 nm and length of 0.4 μm is found growing in the [0002] direction. The distance

between parallel [0002] lattice fringes of the ZnO NW is 2.60 Å, and lattice constants calculated from the SAED pattern (Fig. 5.4 (c)) are a = b = 3.23 Å and c = 5.21 Å, which are consistent with the XRD result. The chemical compositions of ZnO NW in the rectangular box region of Fig. 5.4 (a) were determined by the EDX spectrometer attached to the HR–TEM. Figure 5.4 (d) is the EDX spectrum of ZnO NW and it reveals that zinc (52 %) and oxygen (48 %) are the constituent parts of ZnO NWs.

Upon studying the shape of the ZnO NW, it is found that the NW is straight with a smooth surface and uniform composition. But the morphology of the MZO NW (x = 0.10) (Fig. 5.5 (a)) is quite different from that of ZnO NW. In Fig. 5.5 (a), the MZO NW has blunt tip, and slender root with the diameter of 80 nm and length of 0.5 μm. It is obvious that those MZO NWs grow along the [0002] direction, and the distance between two [0002] lattice fringes of MZO NW is 2.59 Å. The SAED pattern (Fig. 5.5 (c)) can be indexed to the reflection of hexagonal MZO structure, and lattice constants of MZO are a = b = 3.24 Å and c = 5.20 Å. The chemical compositions of this MZO NW (x = 0.1) in the rectangular box regions of Fig. 5.5 (a)were analyzed by the EDX spectrum (Fig. 5.5 (d)), which shows that its chemical composition is zinc (41 %), magnesium (11 %) and oxygen (48 %). Hence, the MZO NW could be synthesized by hydrothermal method with blunt tip, slender root and uniform chemical composition.

Room temperature transmission spectra of the MZO NWs (0 ≤ x ≤ 0.25) fabricated on the glass substrates were recorded by a UV–visible spectrometer (Fig. 5.6 (a)). As shown in the figure, the transmittances of MZO NWs (0 ≤ x ≤ 0.2) are 50 to 60 % under the range from 380 to 600 nm and the UV light is absorbed by these NWs. These transmittances are lower than the MZO films reported by other groups.[163] It is believed that the rough surface of MZO NWs scatters a part of the light causes the transmittance of these samples to decrease. The transmittance of MZO NWs (x =

0.25) is increased to 75% for the shorter nanowires and fewer number density of NWs. One sharp absorption edge appears in the ZnO NWs, while two absorption steps could be observed in these MZO NWs. While the first absorption edge of MZO NWs shifts from 375 to 305 nm, the second absorption edge results from the ZnO buffer layer on the glass substrates in the range from 360 to 365 nm. To realize the relationship between the transmission spectra and the band gap, the absorption coefficient α is estimated after considering the reflection loss of the glass substrate and α^2 is plotted as a function of photon energy (hv) as shown in Fig. 5.6 (b). The absorption edge is used to determine the energy band gap (E_g) of MZO NWs. The band gap of MZO NWs as a function of Mg content is shown in Fig. 5.6 (c). The band gap of ZnO NWs synthesized by hydrothermal method is 3.21 eV, which then increases to 3.95 eV for the MZO (x = 0.25) NWs. With the increase of the Mg content in MZO NWs, the band gaps of MZO NWs increase because of the broadening effect which take place as the carriers feel different potentials for the local concentration of the substituting elements in the crystal. Therefore, by adding various Mg contents in the MZO NWs, the band gap can be modulated. Similar lattice constants of MZO and ZnO could be exploited for the fabrication of MZO/ZnO nanowire heterojunction, which may be used in various optoelectronic applications.

Figure 5.7 shows the photoluminescence spectra of MZO NWs with x = 0, 0.05, 0.10, 0.15, 0.20 and 0.25, respectively. These NWs were excited by a Xe lamp (λ = 325 nm) at room temperature. As, shown in Fig. 5.7 (a), ZnO NWs emit a strong emission at 406 nm (3.05 eV), luminescence at 465 nm (2.66 eV), 495 nm (2.52 eV) and 520 nm (2.38 eV). The UV emission is due to band–edge emission of ZnO, and the band edge emission peak shifts from 406 to 397 nm (3.12 eV) as the Mg content increases to 0.25 in the MZO NWs (Fig. 5.7 (b)). This UV–photoluminescence characteristic reveals the Stokes shift of the solid solution.[190] The band edge emission

intensity of ZnO NWs is the highest; while that of MZO NWs is getting lower as the Mg content increases. It can be demonstrated that the randomly distributed MZO NWs scattered the emission of light that results in the weaker optical intensity. As the Mg content increases up to 0.25, the weakest band edge emission intensity appears due to the shorter optical cavities provided by the NWs. Furthermore, there is a blue emission located at 465 nm in the MZO NWs ($0 \leq x \leq 0.25$). This emission of 465 nm may be associated with the oxygen–deficiency in these NWs.[154,186] The oxygen–deficiency is related to the growth condition of these NWs in the aqueous solution. The MZO NWs grow on the seeding layer while HMTA releases OH$^-$ slowly in the solution. The OH$^-$ ions are finite, but metal ions, such as Zn^{2+} and Mg^{2+}, are sufficient in this environment. Therefore, oxygen is lacking in the MZO NWs fabricated by hydrothermal method. It has been reported that the luminescences at 495 nm and 520 nm of ZnO are caused by the deep–level[187] and singly ionized oxygen vacancies[188]. After annealing at 300 ^{o}C in the oxygen atmosphere, the location of band edge emission is unchanged, but the emission expected to be caused by oxygen–deficiency, deep–levels and singly ionized oxygen vacancies of these MZO NWs ($0 \leq x \leq 0.25$) are decreased because these defects are removed after annealing in the oxygen atmosphere without phase separation.

5.1.2 Electrical characterization

Field emission characteristics of the MZO NWs ($0 \leq x \leq 0.25$) are shown in Fig. 5.8. As shown in the figure, the ZnO NWs on the ITO substrate performs the better field emission property. The turn on electric field (E_{on}) and threshold electric field (E_{th}) under the current density of 1.0 mA/cm^2 of ZnO NWs are 1.6 and 2.1 V/μm, respectively. As the Mg content increases, the E_{on} and E_{th} of the MZO ($0.05 \leq x \leq$

0.25) NWs increase. The Fowler–Nordheim (F–N) plot for ZnO NWs on ITO glass is depicted in the inset of Fig. 5.8, indicating that the measured data fit to the following relationship:

$$\ln\left(\frac{J}{E^2}\right) = \left(\frac{-B\phi^{3/2}}{\beta}\right)\left(\frac{1}{E}\right) + \ln\left(\frac{A\beta^2}{\phi}\right)$$

[5.1]

where J is the current density, E the applied field, ϕ the work function of the emitter, β the field enhancement factor, $A = 1.56 \times 10^{-10} (AeVV^{-2})$ and $B = 6.83 \times 10^3 (VeV^{-3/2}$ μm^{-1}). The β of these samples can be calculated from the slopes of the F–N plots by adopting work function of ZnO (5.37 eV).[191] The β values of MZO NWs with Mg content of 0, 0.05, 0.10, 0.15, 0.20 and 0.25 are 3340, 2753, 2688, 2644, 2489 and 2214, respectively. The β value decreases as the Mg content increases. It is suggested that the ZnO NWs on the ITO glass substrate with acicular tips provided the larger field enhancement factor, while the blunt–tip MZO NWs contribute to smaller field enhancement factor. With the Mg content increasing up to 0.25, the low emission current density is observed for the fewer low-aspect-ratio emitters on the substrate. Based on the previous studies reported by our group[136], the vapor-liquid-solid (VLS) synthesized ZnO NWs exhibit the better field emission properties than the hydrothermal synthesized ones because of the higher aspect ratio and smaller tip diameter. However, the applications of VLS synthesized NWs are restricted since it is difficult to integrate the VLS process to the microelectric devices for the non-uniformity and high reaction temperature. As a result, the hydrothermal synthesized ZnO NWs are suitable material for the electric and electrooptical devices.

5.1.3 Conclusions

In summary, the single crystalline $Mg_xZn_{1-x}O$ nanowires ($0 \leq x \leq 0.25$) on the glass substrates are synthesized by hydrothermal route at 75 to 105 ^{o}C. The crystal structure of MZO NWs is similar to ZnO NWs, while the morphology of MZO NWs is slightly different from the ZnO NWs. Room temperature transmission spectra illustrated that the band gap of MZO NWs shift from 3.21 to 3.95 eV, and the band edge emission from 406 to 397 nm by adding various amounts of Mg in the ZnO NWs. Furthermore, the ZnO NWs with the acicular tips exhibit the better emission properties than MZO NWs. Therefore, the low temperature synthesized MZO NWs with modulated band gap and similar crystal structure to ZnO MWs may be appropriate for fabricating MZO/ZnO nano–heterojunction optoelectronic and field emission devices.

5.2 Influence of P Dopant on MgZnO Nanowires

5.2.1 Structural analysis

The typical FE–SEM images which illustrate the surface morphologies of MZO and PMZO NWs on *p*-type Si substrates are shown in Fig. 5.9. It is indicated that the randomly oriented MZO NWs have an average diameter of 50 nm, an average length of 0.5 μm and a number density of 3.4×10^{10} cm^{-2}. These NWs are non–vertical and randomly distributed over the polycrystalline ZnO seeding film and exhibit homogeneous morphologies with hexagonal columnar shape. The surface morphologies of PMZO NWs (Figure 5.9(b)) including shape, diameter, length and number density are identical to those of MZO NWs. Thus, the surface morphologies of the MZO NWs unchanged after the PH$_3$ plasma treatment.

The crystal structure and phase of the NWs were determined by XRD. Figure 5.10 depicts the XRD patterns of MZO and PMZO NWs grown on the *p*-type Si substrates, respectively, and the inset is the enlarged XRD patterns of peak (002) of the NWs with 2θ from 34 ^{o} to 35 ^{o}. The XRD peak at 33.06^{o} is caused by the Si substrate, and three main diffraction peaks are indexed as (100), (002) and (110) of the wurtzite structure, respectively. Thus, single phase MZO and PMZO NWs with the wurtzite structure were synthesized by the hydrothermal method. The lattice constants and corresponding cell volumes ($3\sqrt{3}a^2c/2$) of MZO and PMZO NWs can be calculated from their XRD patterns. The c–axis lengths calculated from the (002) peak of MZO and PMZO are 5.192 and 5.198 Å, respectively; a–axis length calculated from the (100) peak is 3.241 Å for both NWs, and the cell volumes are 141.69 and 141.86 Å^{3}, respectively. After the P plasma treatment, the PMZO NWs retain the crystal structure of wurtzite and no other impurities appear but have a small

change in the c–axis length and slight increase in cell volume. The variation of c-lattice constant may be due to the P plasma implanting perpendicularly to the substrate. Such a P implantation along the (002) direction of MZO leads to an increase in the c-axis parameter. The addition of P to MZO forms a solid solution with the wurtzite structure, a possible reaction is

$$P''' \xrightarrow{\ (Mg,Zn)O\ } P_O' + V_{(Mg,Zn)}'' \qquad\qquad [5.2]$$

where P_O' means P^{3-} substituted for O^{2-} site and $V_{(Mg,Zn)}''$ indicates a vacancy formed at a Zn^{2+} or Mg^{2+} site in the lattice of the MZO NWs. It is suggested that a P^{3-} ion is substituted for an O^{2-} ion, which leads to a Zn vacancy formation. Therefore, the deviation of the lattice constants can be due to the P atoms incorporated in the NWs by plasma implantation and the different ionic radii between P^{3-} (r_P^{3-} =1.06 Å) and O^{2-} (r_O^{2-} =0.73 Å).
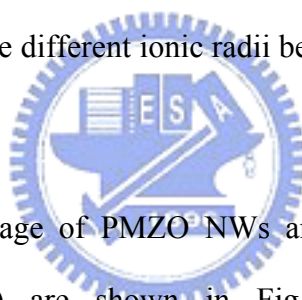
The typical HRTEM image of PMZO NWs and corresponding selected area electron diffraction (SAED) are shown in Fig. 5.11, which illustrates the microstructural features of the PMZO NWs. The SAED pattern in the inset of Fig. 5.11 can be indexed to the reflection of single crystalline PMZO hexagonal structure, and its lattice constants are a = b = 3.241 Å and c = 5.198 Å, which are consistent with the XRD result. The SAED pattern indicates that the NWs grow in the [0002] direction with wurtzite structure, and the distance between parallel [0002] lattice fringes of the NWs is 5.198 Å. This pattern also depicts the single crystalline structure of the PMZO NWs. Moreover, the defects such as dislocations and stacking fault were not observed in the PMZO NWs. For both the MZO and PMZO NWs, only the growth direction [0002] was found. It concludes that the MZO NWs can be doped with P by the plasma treatment but without damaging its crystal structure.

The chemical composition of the PMZO NWs was further analyzed by the XPS and the results are shown in Fig. 5.12. The XPS spectrum of PMZO NWs shows that there are feature peaks corresponding to elements of Zn, Mg, P, O, C and Si. Three strong peaks located at 530.8, 1024.4 and 1048.0 eV are respectively due to the O (1s) and Zn ($2p_{3/2}$ and $2p_{1/2}$) binding energies for ZnO NWs, while three weak peaks located at 49.6, 129.9 and 130.5 eV are owing to the Mg (2p) and P ($2p_{3/2}$ and $2p_{1/2}$) binding energies for Mg and P incorporated in the NWs. The appearance of carbon at the peak of 263 eV is resulted from the residual reactants adsorbed on the surface of the NWs, and the peak of Si was detected due to the Si substrate. Obviously, the dominant chemical composition of the NWs is ZnO and a little amount of Mg and P is incorporated into these NWs on the basis of the results of XPS measurement. With further detailed examinations, the chemical composition of these NWs is $P_{0.02}Mg_{0.1}Zn_{0.9}O$.

Figure 5.13 (a) shows the photoluminescence spectra of MZO and PMZO NWs excited by a Xe lamp ($\lambda = 325$ nm) at room temperature. It is indicated that MZO NWs emit luminescences at 403.8 nm (3.07 eV), 451 nm (2.75 eV), 465 nm (2.67 eV), 495 nm (2.51 eV) and 520 nm (2.38 eV), respectively. The UV emission at 403.8 nm is caused by the band–edge emission of MZO. The luminescence at 451 nm was reported to be due to the Zn–vacancy (V_{Zn}'').[185] The emission of 465 nm may be associated with the oxygen–deficiency in these NWs formed in the growth environment of hydrothermal process.[186] The possible reactions take place in the aqueous solution in such an environment as the followings:

$(CH_2)_6N_4 + 10H_2O \rightarrow NH_4OH + 6HCHO$ [5.3]

$(Zn^{2+}, Mg^{2+}) + 2OH^- \rightarrow (Zn,Mg)O + H_2O$ [5.4]

The Zn^{2+} ions are sufficient in this solution, but the OH^- ions are finite in the

solution due to that the HMTA slowly releases OH⁻. Thus, oxygen is expected to be lacking in the NWs fabricated by the hydrothermal method. This phenomenon also results in the deep–level[187] and singly ionized oxygen vacancies[188] luminescences at 495 nm and 520 nm as shown in Fig. 5.13 (a). On the other hand, the PMZO NWs emit 385.4 nm (3.22 eV), 412 nm (3.02 eV), 451 nm, 465 nm, 480 nm (2.58 eV), 495 nm and 520 nm luminescences. It is shown that the near band edge emission peak shifts from 403.8 to 385.4 nm and a Stokes shift of 0.15 eV happen as the P was incorporated in the MZO NWs. Such a blueshift of optical band to band transitions was reported to be related to the Burstein–Moss effect.[190] The emissions at 412 and 480 nm may be associated with the nonstoichiometric oxide[192] and ionized Zn–vacancy ($V_{Zn}^{'}$)[185] in the PMZO NWs. The UV emission of PMZO NWs is a little weaker than that of MZO NWs, while the emissions of PMZO NWs at 465, 495 and 520 nm caused by oxygen vacancies are much weaker than those of MZO NWs. It could be proposed that the P substitution causes the oxygen vacancies in PMZO decrease and introduces an acceptor level leading to a decrease in electron concentration but an increase in hole concentration and finally PMZO NWs become p-type conduction, which can be further verified by the following Hall effect measurement. Room temperature transmission spectra of MZO and PMZO NWs were recorded by a UV–visible spectrometer. To realize the relationship between the transmission spectra and the band gap, the ($\alpha h v$)$^{1/2}$ is plotted as a function of photon energy ($h v$) as shown in Fig. 5.13(b). The absorption edge is used to determine the energy band gap (E_g) of the NWs. The band gap of MZO NWs is 3.41 eV, and that increases to 3.56 eV for the PMZO NWs. Such an increase is attributed to the broadening effect occurring as the carriers feel different potentials for the different local concentrations of the substituting elements in the crystal. Therefore, the band

gap can be modulated by adding P content in the MZO NWs, which may be applied in various optoelectronic applications.

5.2.2 Electrical characterization

On the basis of the results of the Hall effect measurement, the MZO bulk performs the *n*-type conduction with a resistivity of 1.1 Ωcm, Hall mobility of 10.2 cm^2/Vs and carrier concentration of 5.8×10^{17} cm^3, while the PMZO one exhibits the *p*-type behavior with a resistivity of 4.3×10^{-1} Ωcm, Hall mobility of 15.8 cm^2/Vs and carrier concentration of 9.2×10^{17} cm^3. Therefore, it can be expected that the PMZO NWs also exhibit p-type conductivity due to the same composition between NWs ans bulk materials we measured.

The field emission characteristics of the MZO and PMZO NWs on the *p*-type Si (100) substrate are shown in Fig. 5.14. As shown in Fig. 5.14 (a), the turn on electric field (E_{on}, under the current density of 1.0 μA/cm^2) and threshold electric field (E_{th}, under the current density of 1.0 mA/cm^2) of MZO NWs are 1.3 and 1.9 V/μm, respectively, while those of PMZO NWs are 1.0 and 1.5 V/μm, respectively. The semi-logarithmic plots of *J–E* field emission characteristics shown in the inset of Fig. 5.14(a) further identify their emission properties. These plots can be divided into three parts: zero emission (region 1), Fowler–Nordheim (F–N) field emission (region 2) and current saturation region (region 3). The E_{on} is defined as the electric field for which tunneling occurs of PMZO NWs is 1.0 V/μm which is lower than that of MZO NWs (1.3 V/μm). Above E_{on} (region 2), the emission current density abruptly increases and then saturates at the high electric field region (region 3). The current density emitted by MZO NWs is lower than that of PMZO NWs under the same electric field. A knee electric field, E_{knee}, is defined as the demarcation point between F–N field emission

and current saturation regions. The E_{knee} of MZO and PMZO NWs, respectively, are 1.8 and 1.5 V/μm. In this F–N tunneling region, the better field emission properties were observed for the PMZO as compared with MZO due to the resistance of PMZO is smaller. This worse field emission ability of MZO may be due to a potential barrier formed by the negative charge in the surface state of n-type emitters.[165,166] Thus, the p-type PMZO NWs with lower surface state barrier perform the better field emission properties. The MZO and PMZO NWs on p-type Si substrates perform a saturation region at higher electric field (region 3) in the J-E plot. This saturation region existed is due to the high resistance in series of semiconductor emitters[189]. As shown in the inset of Fig. 5.14 (a), the resistances in series of MZO and PMZO NWs are introduced to fit the J-E plot and the values of 93 and 62 kΩ are obtained, respectively. The decreasing resistance in series of PMZO NWs is attributed to a lower potential barrier formed by the positive charge in the surface state of p-type PMZO emitters. Obviously, the P dopant can improve the field emission properties of MZO NWs on the p-type Si (100) substrate. The PMZO NWs with the low threshold electric field and low resistance in series are suitable for the field emission applications.

The corresponding F–N plots [ln(J/E^2) vs. E^{-1}] of the MZO and PMZO NWs on the p-type Si (100) substrate are depicted in Fig. 5.14(b), indicating that the measured field emission characteristics fit the F–N relationship. The F–N relationship is as follow:

$$J = \frac{A\beta^2 E^2}{\phi} \exp\left(\frac{-B\phi^{3/2}}{\beta E}\right)$$ [5.5]

Where J is the current density, E the applied field, Φ the work function of the ZnO (5.37 eV), β the field enhancement factor, $A = 1.56 \times 10^{-10}$ (AV^{-2} eV) and $B = 6.83 \times 10^3$ ($VeV^{-3/2}$ μm^{-1}). The calculated β value of MZO NWs is 3048, and that of PMZO NWs is 3054. Therefore, the β value of PMZO NWs is close to that of MZO

NWs. It is well known that the β depends on the geometry, structure, tip size and number density of the emitters on the substrate. It is believed that the similar surface morphology and structure between PMZO and MZO NWs (Figs. 5.8-11) is the main reason for having nearly same β values.

The photoenhanced field emission properties of MZO and PMZO under a 30 W incandescent lamp irradiation are studied to demonstrate the influence of the illumination on the field emission. The E_{on}, E_{th}, E_{knee}, β and R_s values of these NWs can be obtained from the slopes and fitting curves of the F–N plots are listed in Table 5.1. The E_{on} and E_{th} of PMZO NWs under illumination decrease to 0.9 and 1.3 V/μm, respectively, and its maximum current density increases to 72 mA/cm^2. As shown in the insert of Fig. 5.14(c), the calculated resistances in series of the MZO and PMZO NWs under illumination from the fitting are 72 and 45 kΩ, respectively, which are lower than those values without illumination. The β values of these two NWs under illumination calculated from the slopes of the F–N plots (Fig. 5.14(d)) are identical to those of the dark one. Therefore, it is demonstrated that the carriers in the MZO and PMZO NWs are excited during the illumination leading to increase the emission current density and reduce the resistance in series, but unchanged structure and surface morphology after illumination lead to similar β values.

Figure 5.15 depicts the *J-E* curves and corresponding F-N plots with E from 0 to 1.95 V/μm (forward sweep) and then back to 0 V/μm (backward sweep) of PMZO NWs grown on the *p*-type Si substrate. The two *J-E* curves are almost merged and no hysteresis behavior caused by adsorbates[193] is observed in this measurement. Thus, it is demonstrated that the good field emission performance (low turn on electric field and high emission current density) of PMZO NWs is not caused by the adsorbates on the NWs but the intrinsic properties of the NWs.

5.2.3 Conclusions

In summary, the single crystalline MZO and PMZO NWs on the *p*-type Si (100) substrates are synthesized by hydrothermal route. The structure and surface morphology of MZO NWs are similar to those of PMZO NWs. The average diameter of these two nanostructures is 50 nm and the length is 500 nm. Room temperature transmission spectra illustrated that the band gap of MZO NWs shifts from 3.41 to 3.56 eV, and the band edge emission from 403.8 to 385.4 nm when the plasma implantation of P into them to form PMZO NWs.. Moreover, such PMZO NWs exhibit better field emission properties including the lower threshold electric field, lower resistance in series and higher emission current density, in comparison with MZO NWs. The improved field emission characteristic of PMZO is attributed to the changes in surface state of the nanostructure at both threshold voltage and F–N field emission regions. The PMZO NWs with good field emission properties is a suitable material for flat display application. Moreover, the modulated band gap can be obtained with P doping but keep similar crystal structure, which may also be able to be applied for the future nano–homojunction ZnO optoelectronic and field emission devices.
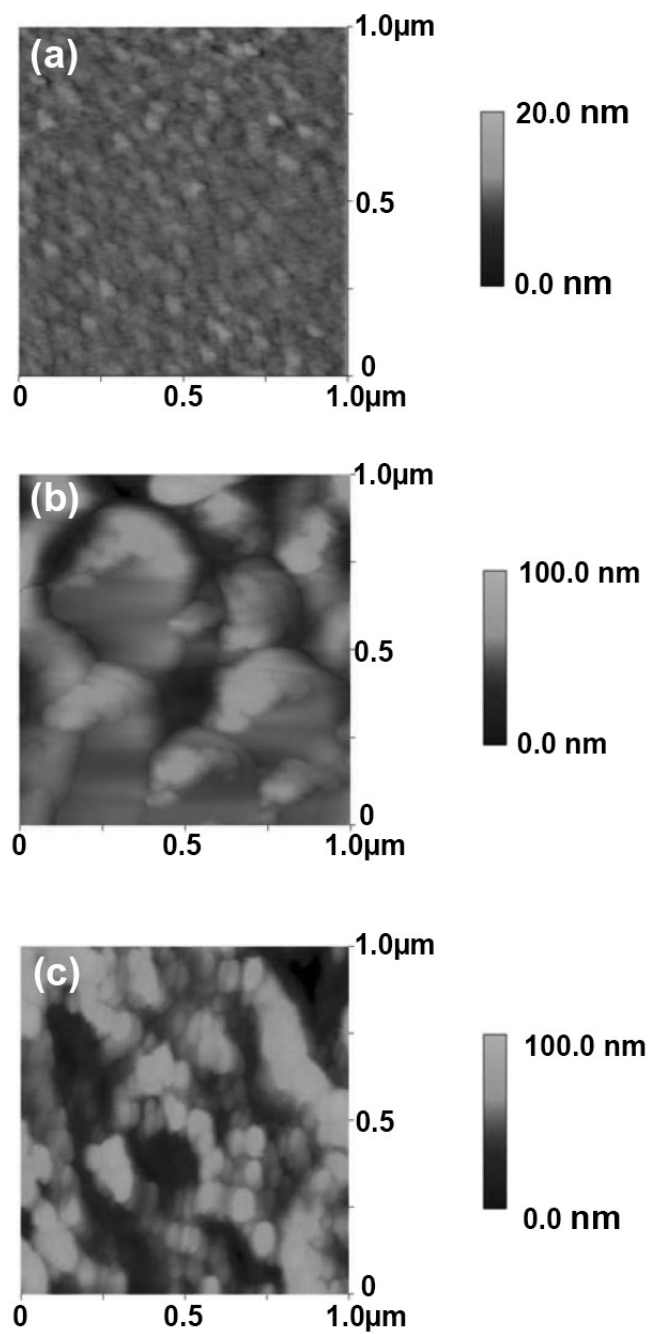
Figure 5.1 AFM micrographs of (a) as–deposited ZnO seeding layer surface, (b) 10 min. hydrothermal–grown ZnO surface, (c) 10 min. hydrothermal–grown MZO (x = 0.10) surface.
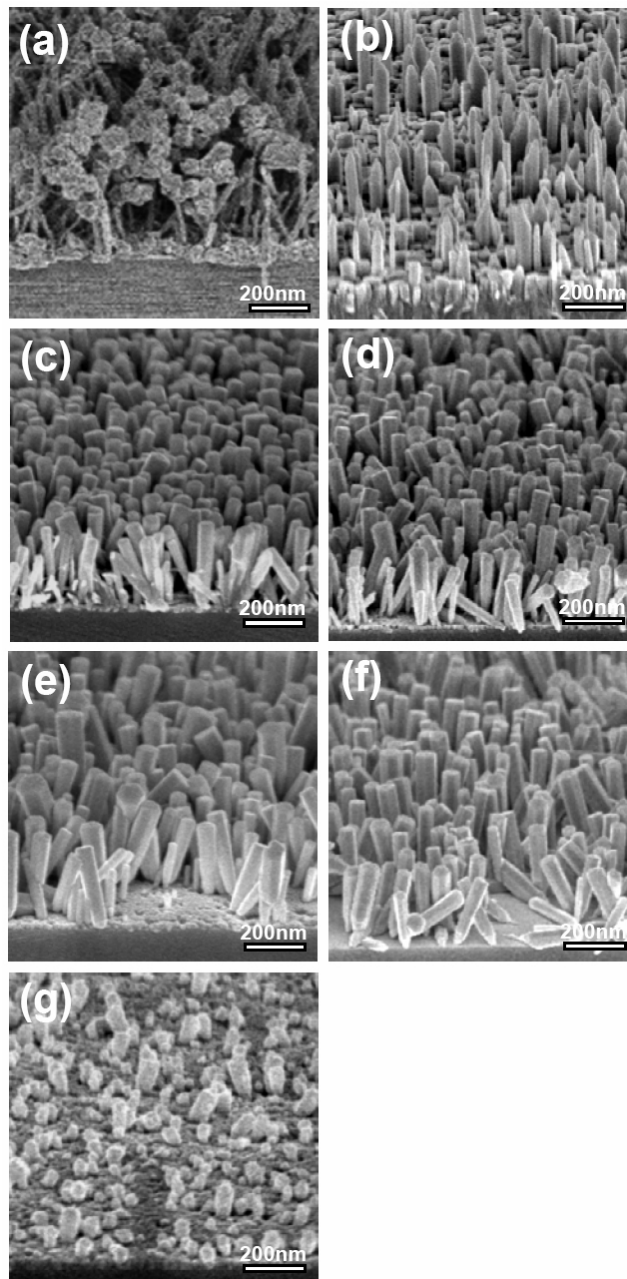
Figure 5.2 (a) Cross–section FE–SEM micrographs of as-grown ZnO NWs, and the morphologies of MZO NWs with various x (b) x = 0, (c) x = 0.05, (d) x = 0.10, (e) x = 0.15, (f) x = 0.20, and (g) x = 0.25.
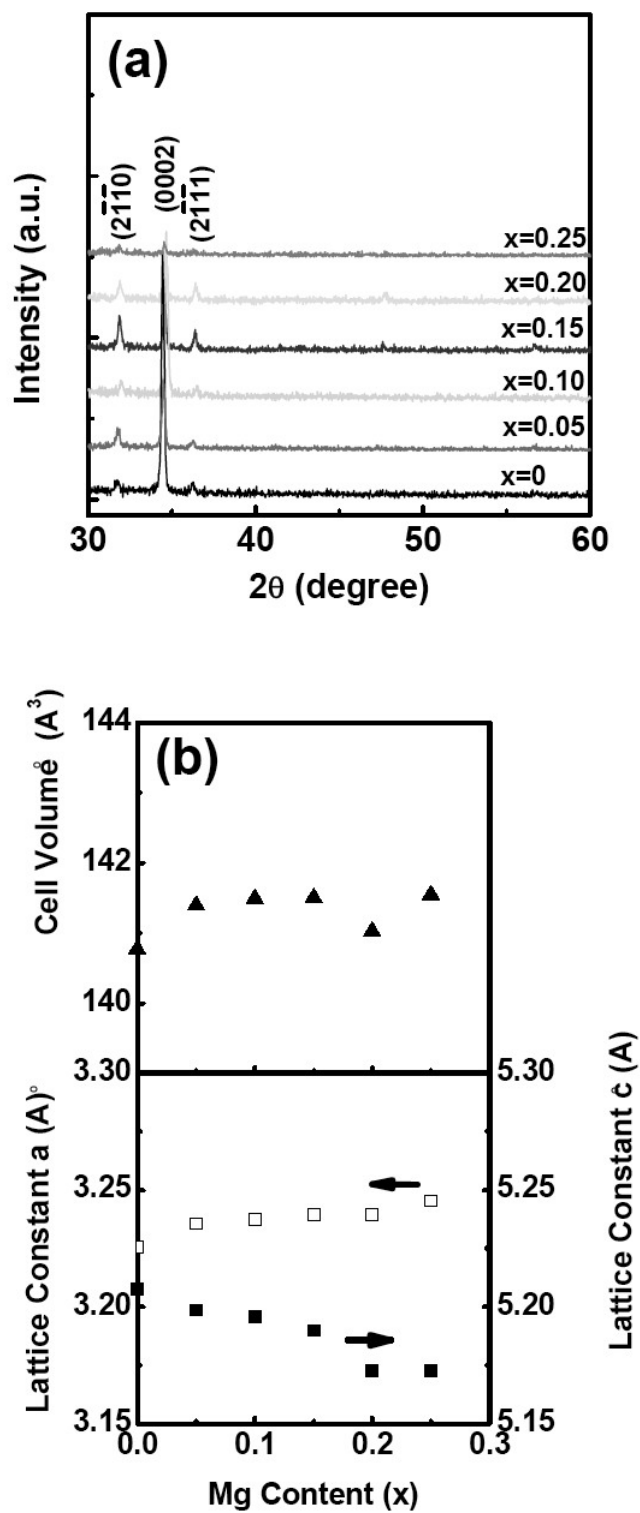
Figure 5.3 (a) XRD spectra of MZO NWs with various x indicated. (b) a– and c– axis lattice parameters and cell volume of MZO NWs.
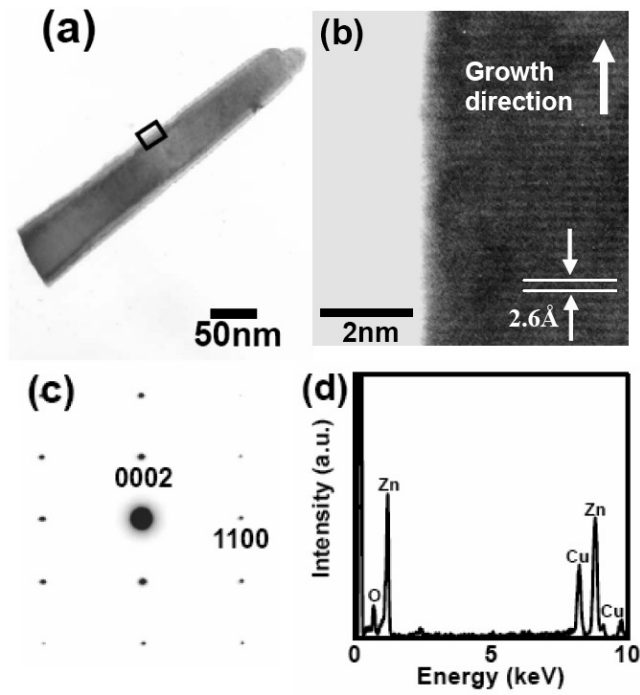
Figure 5.4 (a) TEM micrograph of ZnO NWs. (b) HR–TEM image of ZnO NWs in the rectangular box region in (a). (c) SAED of ZnO NWs marked in the boxed region of (a). (d) EDX spectra of ZnO NW in the marked region of (a).
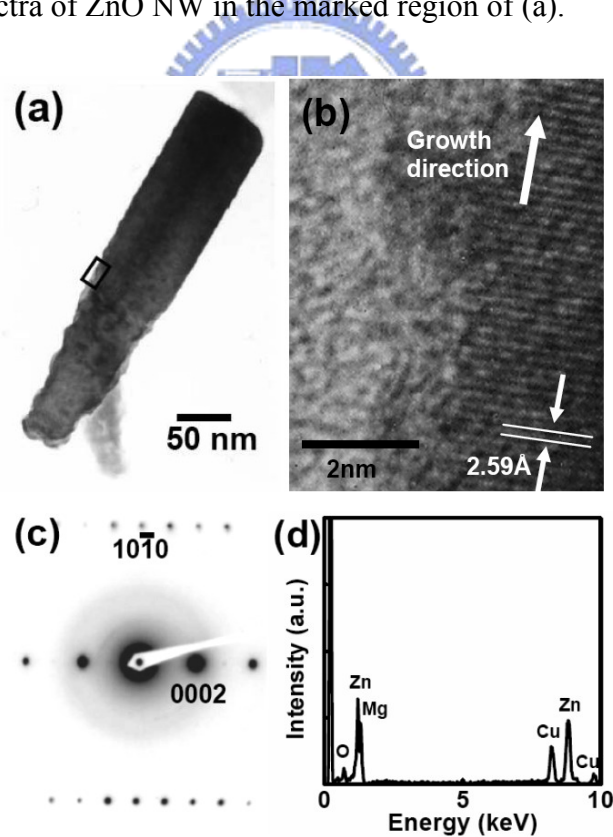
Figure 5.5 (a) TEM micrographs of MZO (x = 0.1) NWs. (b) HR–TEM image of MZO NWs in the rectangular box region of (a). (c) SAED of the MZO NWs of the marked box region of (a). (d) EDX spectra of the MZO NW in the boxed region of (a).
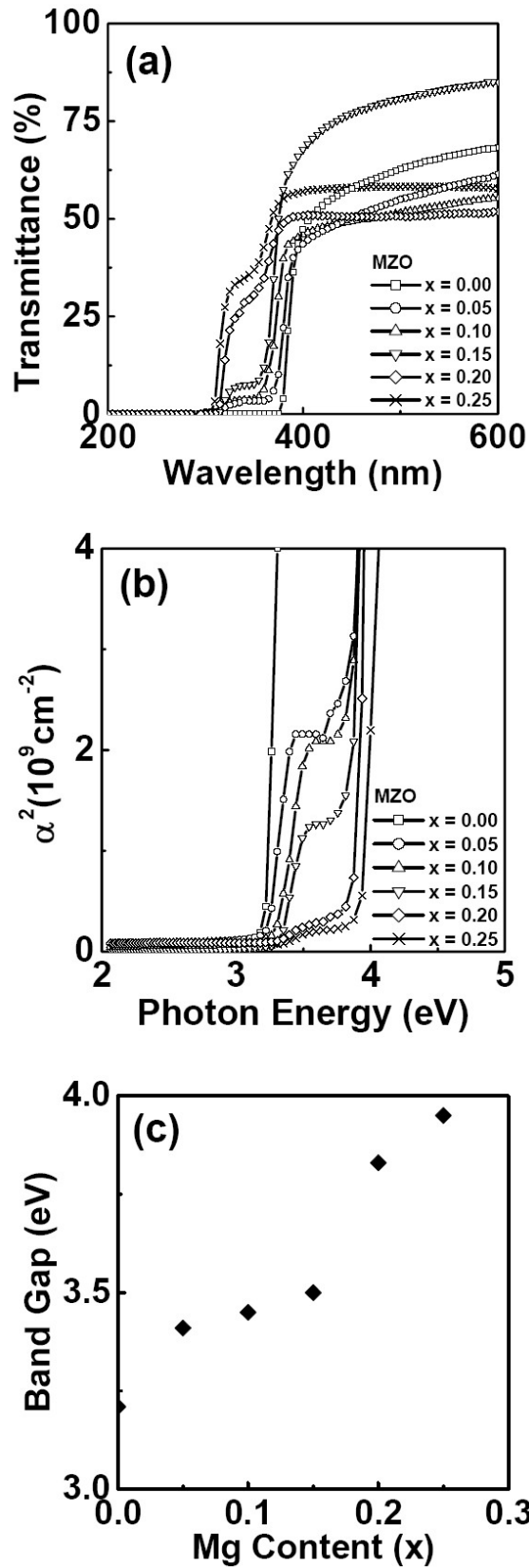
Figure 5.6 (a) UV−VIS transmission spectra of MZO ($0 \leq x \leq 0.25$) NWs. (b) A plot of α^2 vs. photon energy for MZO ($0 \leq x \leq 0.25$) NWs. (c) energy band gap as a function of Mg composition.
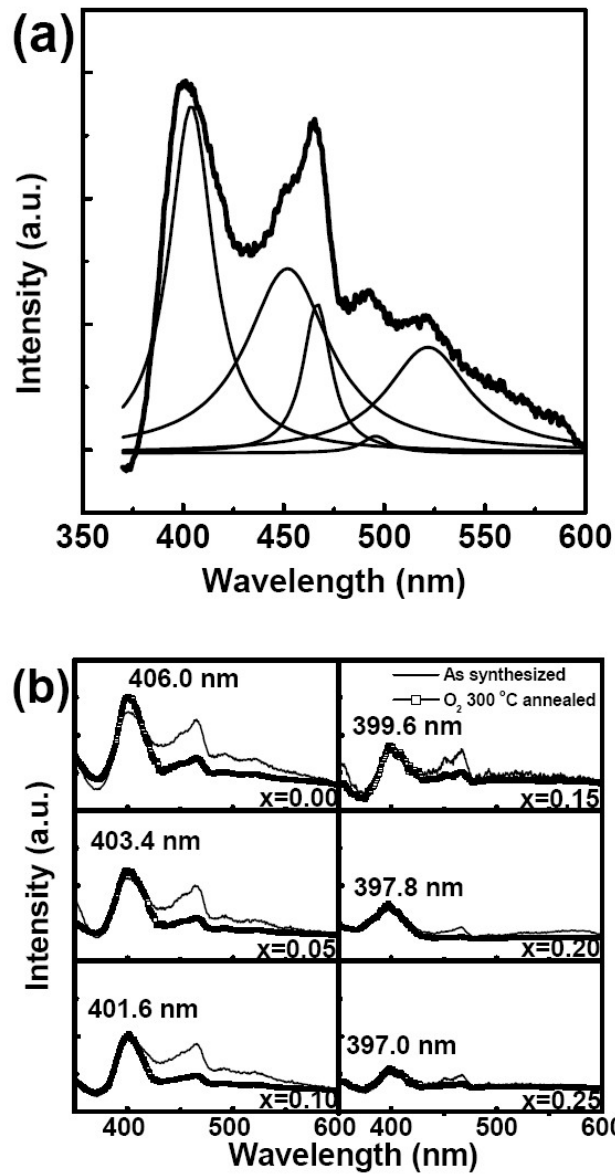
Figure 5.7 (a) PL spectra of ZnO NWs and deconvolution of the spectra. (b) PL spectra of as synthesized and 300 $^{\circ}$C O$_2$ annealed MZO ($0 \leq x \leq 0.25$) NWs.
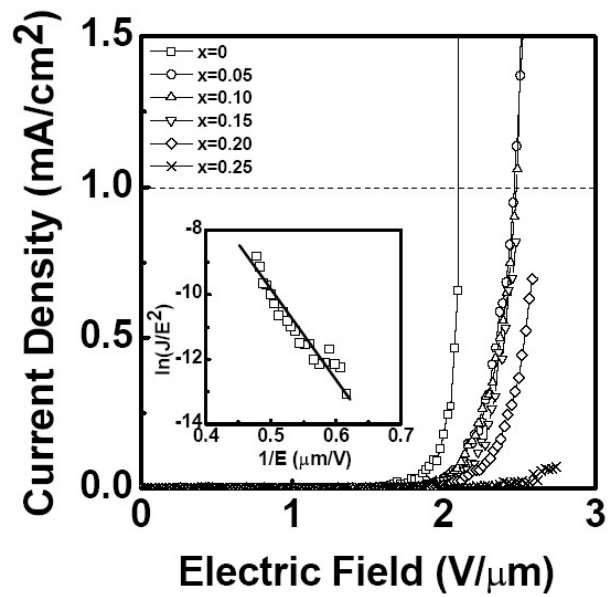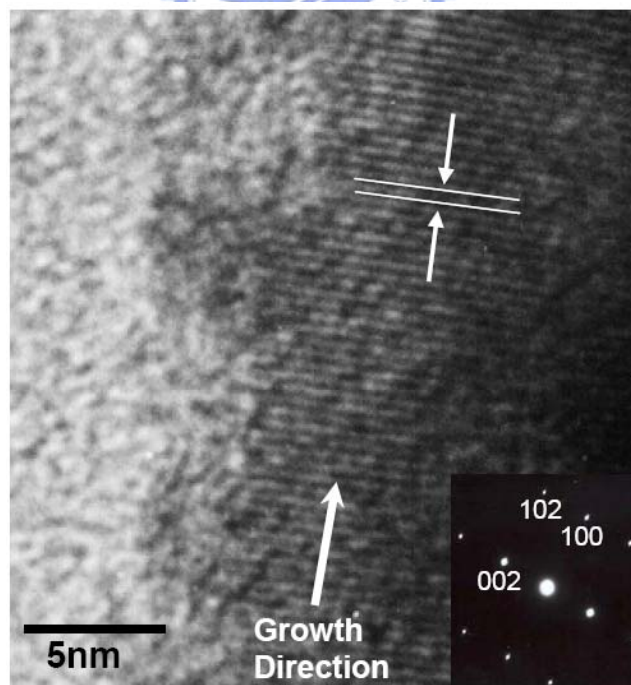
Figure 5.8 Field emission current–voltage curves of MZO ($0 \le x \le 0.25$) NWs. (The inset is the Fowler–Nordheim plot of ZnO NWs)
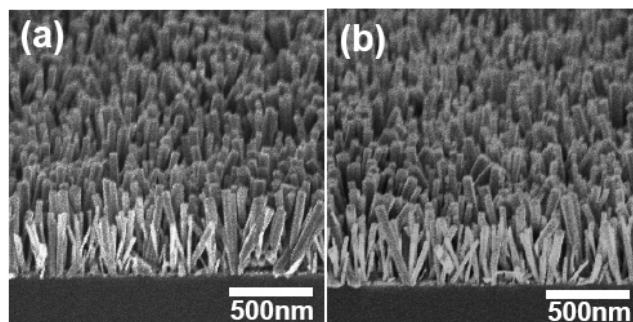
Figure 5.9 Cross section FE–SEM micrographs of (a) MZO NWs, (b) P-MZO NWs grown on Si substrates.
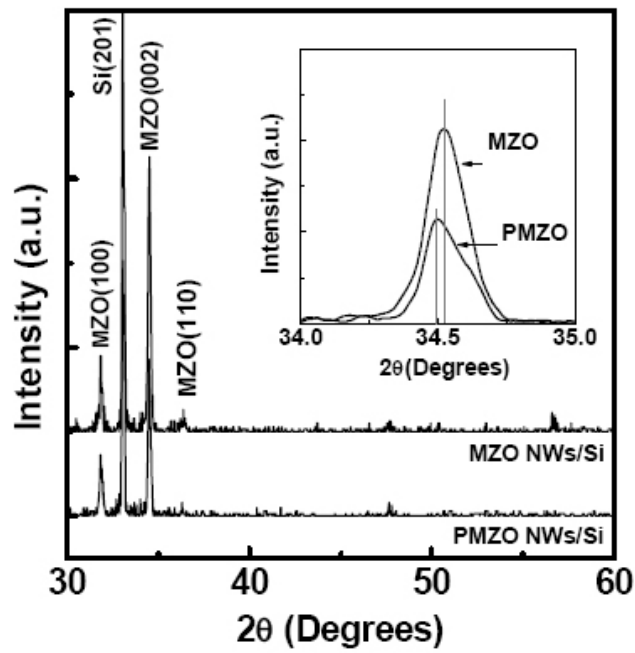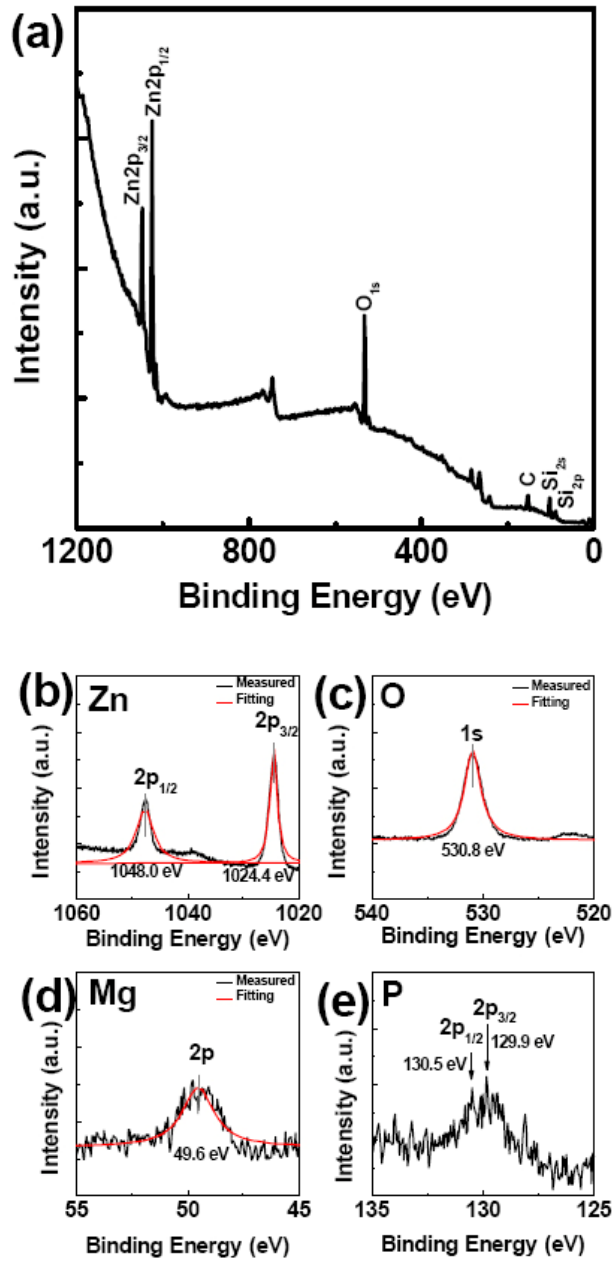
Figure 5.10 XRD patterns of (a) MZO NWs and (b) PMZO NWs grown on Si substrates. The inset is the enlarged patterns with 2θ from 34 ^{o} to 35°.
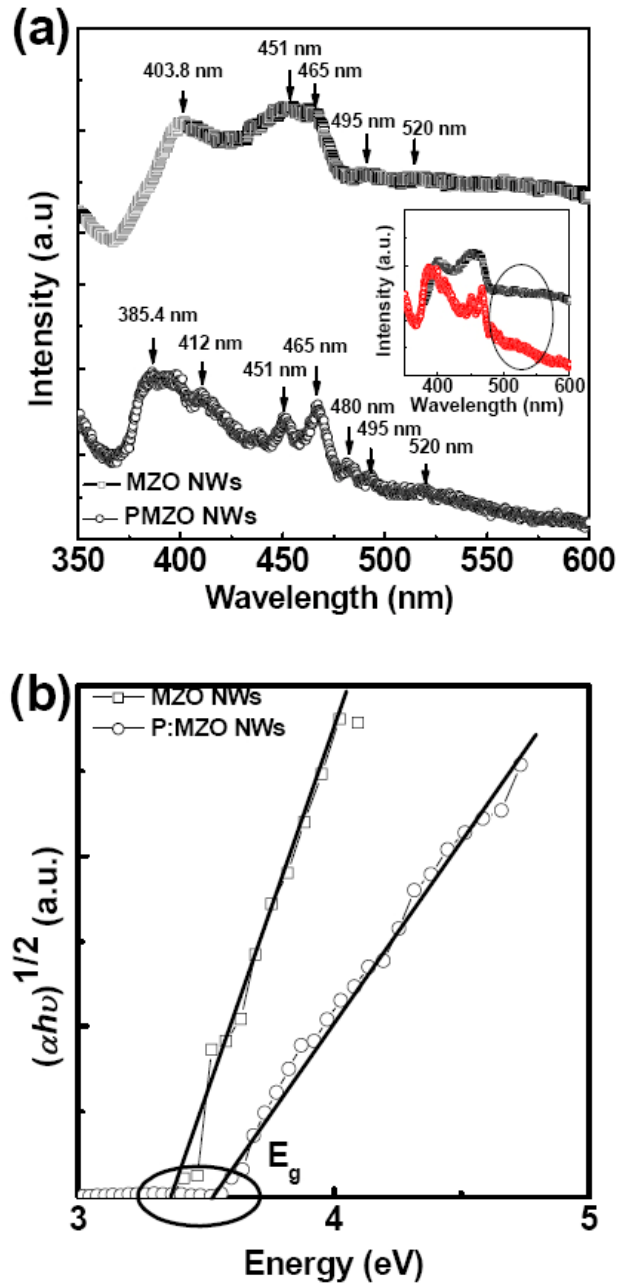

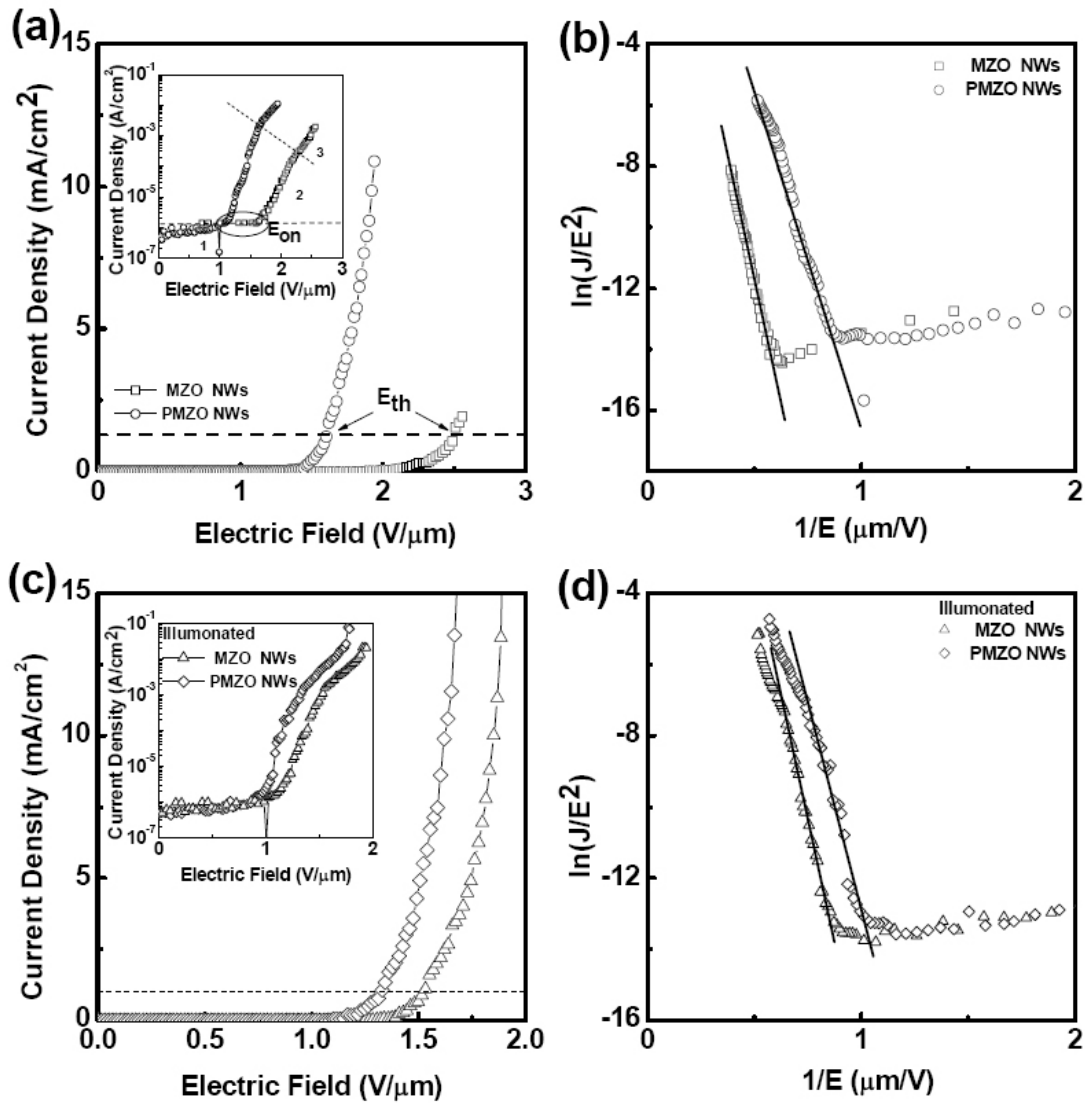**Figure 5.11** HRTEM micrograph of PMZO NWs. The inset is the corresponding SAED of the NWs.

Figure 5.12 (a) XPS spectrum of PMZO NWs, (b) Zn spectrum, (c) O spectrum, (d) Mg spectrum and (e) P spectrum.

Figure 5.13 (a) PL spectra of MZO and PMZO NWs. (b) Tauc's plots of MZO and PMZO NWs.

Figure 5.14 (a) Field emission *J–E* curves of MZO and PMZO NWs grown on *p*-type Si substrate. The inset is the semi-logarithmic *J–E* plot and resistance in series fitting. (b) The corresponding F–N [ln(*J/E²*) vs. *E⁻¹*] plots of the NWs. (c) Photoenhanced field emission characteristics of MZO NWs and PMZO NWs grown on Si substrates. The insert is the fitting of resistance in series. (d) Corresponding F–N plots.
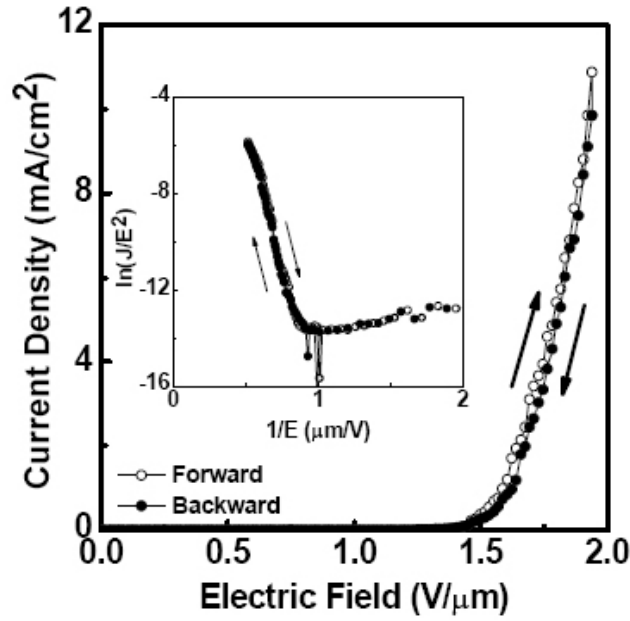
Figure 5.15 Field emission *J–E* curves of PMZO NWs with forward and backward sweeps. The inset depicts the corresponding FN plot.

Table. 5.1 E_{on}, E_{th}, E_{knee}, β and R_s values of MZO NWs and PMZO NWs grown on the Si substrates with and without illumination.

	MZO		PMZO	
	Dark	Illuminated	Dark	Illuminated
E_{on}(V/μm)	1.3	1.0	1.0	0.9
E_{th}(V/μm)	1.9	1.5	1.5	1.3
E_{knee}(V/μm)	1.8	1.6	1.5	1.4
B	3048	3049	3054	3058
R_s(kΩ)	93	72	62	45